Volume 10
Number 10
October 2023
Pages 2613–2926

Environmental Science Nano

rsc.li/es-nano

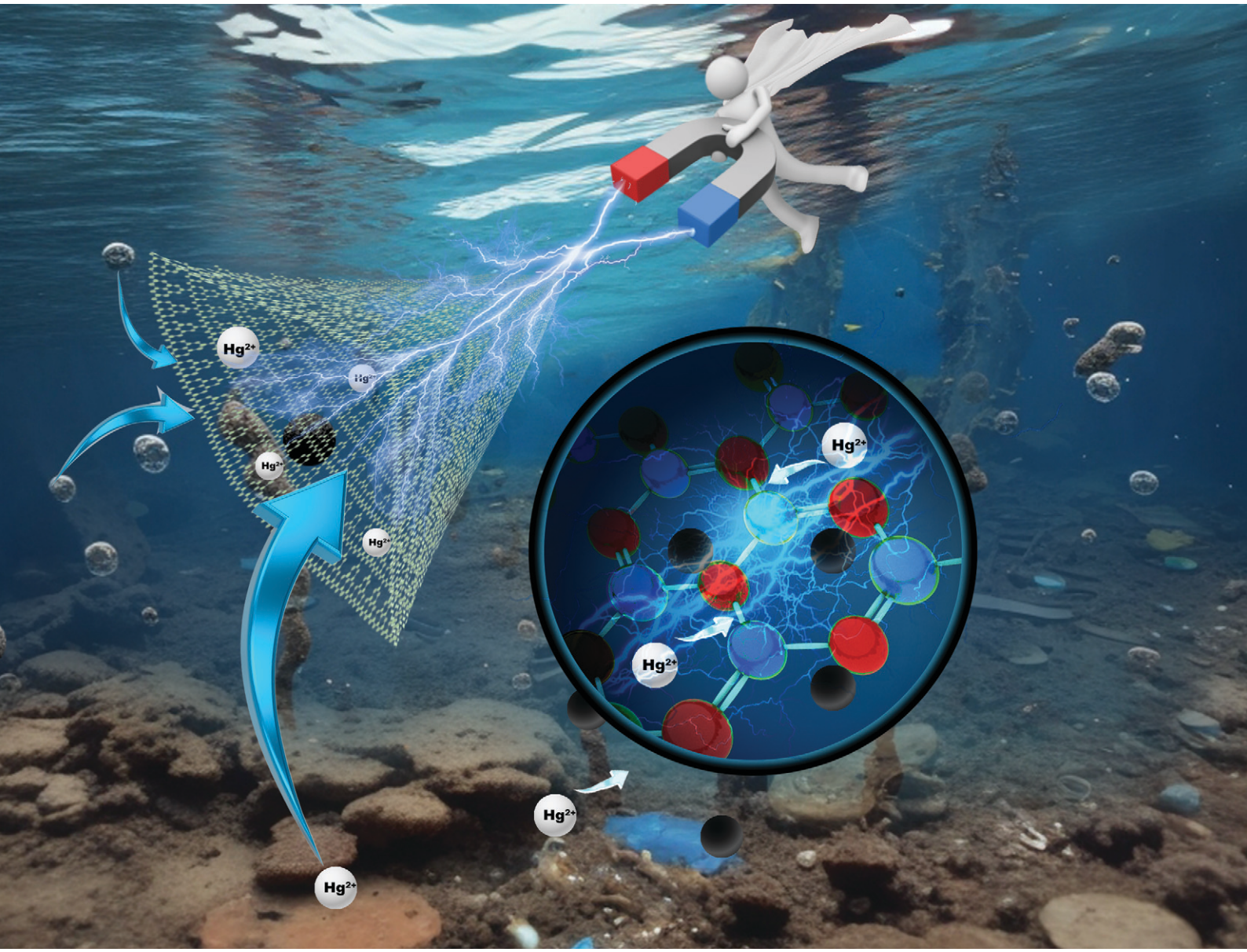

ISSN 2051-8153

ROYAL SOCIETY OF CHEMISTRY

PAPER

Raghuraj Singh Chouhan, Sonu Gandhi, Ivan Jerman, Milena Horvat *et al.*
Green synthesis of a magnetite/graphitic carbon nitride 2D nanocomposite for efficient Hg^{2+} remediation

Environmental Science Nano

ROYAL SOCIETY OF CHEMISTRY

PAPER

View Article Online
View Journal | View Issue

Cite this: *Environ. Sci.: Nano*, 2023, **10**, 2658

Green synthesis of a magnetite/graphitic carbon nitride 2D nanocomposite for efficient Hg^{2+} remediation†

Raghuraj Singh Chouhan, *[a] Jan Gačnik,[a] Igor Živković, [ab] Sreekanth Vijayakumaran Nair,[ab] Nigel Van de Velde,[c] Alenka Vesel,[d] Primož Šket,[e] Sonu Gandhi,*[f] Ivan Jerman *[c] and Milena Horvat*[ab]

Novel nanoadsorbents demonstrate the potential to efficiently eliminate harmful substances, such as Hg^{2+}, from the environment while preserving ecological balance. However, the search for environmentally-friendly nanomaterials as ideal adsorbents, as well as the development of suitable synthesis protocols, remains a challenge. This study presents an effective thermal-sonication technique for producing unique *de novo* tris-*s*-triazine carbon nitride nanosheets decorated with magnetite nanoparticles (M-g-CN). The structural integrity and chemical properties of the M-g-CN nanocomposite were extensively characterized using a battery of analytical instruments, including FTIR, SEM, TEM, XRD, XPS, AFM, Raman, and NMR. The obtained data, along with the analysis results, are discussed in detail. The novel synthesis method yields a high percentage (97.7%) of stable, highly selective, and reusable M-g-CN (40 mg mL^{-1}). The resulting M-g-CN effectively binds Hg^{2+}, with binding efficiencies of 96.0%, 97.5%, 98.2%, and 99.4% for Hg^{2+} concentrations of 50 pg mL^{-1} in marine, stream, precipitation, and ultra-pure matrices, respectively. Also, the magnetite-decorated particles can be easily retrieved using an applied magnetic field. This greener and scalable synthesis method does not require harsh chemicals, making it cost-effective, eco-friendly, and non-toxic compared to other technologies such as carbon filters, ion exchange resins, chemical precipitation, membrane filtration, electrochemical methods, and biological remediation. Overall, the synthesized M-g-CN exhibits wide-ranging potential applications, particularly as a green adsorbent in passive samplers or materials for remediation purposes.

Received 7th June 2023,
Accepted 30th June 2023

DOI: 10.1039/d3en00367a

rsc.li/es-nano

Environmental significance

Mercury is considered one of the top ten most hazardous chemicals, posing a significant threat to public health. Fortunately, several international directives regulate mercury emissions, with the Minamata Convention (2013) being the most well-known. However, a need remains to develop new technologies that can safely capture mercury until the impact of such regulations on anthropogenic Hg emissions can be observed. This need has stimulated our research into the green synthesis of magnetite-decorated graphitic carbon nitride (M-g-CN) nanocomposites, which are highly effective at capturing and removing inorganic mercury from various aqueous matrices. The material's unique magnetic properties enable easy separation from the water matrix using strong magnets, thereby facilitating mercury removal. Additionally, the material can be reused multiple times.

[a] *Department of Environmental Sciences, Jožef Stefan Institute, Jamova Cesta 39, 1000 Ljubljana, Slovenia. E-mail: raghuraj.singh@ijs.si, milena.horvat@ijs.si*
[b] *Jožef Stefan International Postgraduate School, Jamova Cesta 39, 1000 Ljubljana, Slovenia*
[c] *National Institute of Chemistry, Hajdrihova 19, 1000 Ljubljana, Slovenia. E-mail: Ivan.Jerman@ki.si*
[d] *Department of Surface Engineering, Jožef Stefan Institute, Jamova 39, 1000 Ljubljana, Slovenia*
[e] *Slovenian NMR Center, National Institute of Chemistry, Hajdrihova 19, 1000 Ljubljana, Slovenia*
[f] *DBT-National Institute of Animal Biotechnology (DBT-NIAB), Hyderabad, Telangana 500032, India. E-mail: gandhi@niab.org.in*
† Electronic supplementary information (ESI) available. See DOI: https://doi.org/10.1039/d3en00367a

1. Introduction

The industrialization of society has many negative ecological consequences, including releasing toxic elements into the environment.[1,2] One such element is mercury (Hg), a highly toxic transition element that poses a significant public health problem.[3] Mercury naturally exists in the Earth's biogeochemical system and is emitted during volcanic and geological activities.[4,5] Human activity also releases significant amounts of mercury into the environment. For example, 2200 tonnes of anthropogenic mercury were emitted into the atmosphere in 2015 alone.[6] Anthropogenic sources include

cement production plants, artisanal gold mining, coal burning, metal production, and during the chlor-alkali process.[7–9]

In the environment, mercury is present in several chemical forms, the most common being inorganic mercury (iHg/Hg^{2+}), gaseous elemental mercury (GEM or Hg(0)), and monomethyl mercury (CH_3Hg^+, denoted here as MeHg). The primary route of human exposure to Hg(0) is inhalation, while iHg and MeHg are mainly ingested through food consumption. The organic Hg species can also bioaccumulate and become biomagnified up the food chain to levels that potentially risk the well-being of humans[9] and wildlife.[10]

At present, mercury emissions are regulated by different directives such as the EU's industrial emission, air quality, waste incineration regulations (2010/75/EU, 2004/107/EC, 2000/76/EC), and globally through the Minamata Convention (2013), which 128 countries have now signed.[11] Nevertheless, given the inability to observe the effects of reduced anthropogenic Hg emissions/releases, it is crucial to develop new technologies for capturing mercury from the aquatic environment for remediation and monitoring. As a result, this requirement has stimulated researchers to design and synthesize novel adsorbent materials.[12–16]

Several technological approaches have been developed and implemented to capture toxic metals, including ion exchange, membrane filtration, extraction, reverse osmosis, adsorption, and irradiation.[12,17] Among these, adsorption is considered the best option because of its cost-effectiveness, efficiency, ease of preparation, and eco-friendly properties.[18] Such materials include clay minerals, polymers, nanowires, composites, metal–organic framework and zeolites.[19–24] Despite this, eliminating harmful ions remains challenging, and much research has gone into improving the material properties of adsorbents. One approach in this direction involves capitalizing on the interaction between thiol groups (–SH) and mercury to develop various adsorbent materials.[15] Several groups reported –SH-based adsorbent materials, including clays,[25] activated charcoals,[26] mesoporous silica,[27] cross-linked materials, and poly-ethyleneimine.[28] These materials show excellent binding properties but lack a relatively high surface area, functional groups, and small pore sizes. Hybrid nanomaterials have gained the attention of researchers in recent years for removing toxic metals form aqueous matrices, due to their unique properties and enhanced performance.[29–32] However, cost, scalability, stability, selectivity, regeneration, disposal and performance in complex aqueous matrices limits their widespread applications. Similarly, other materials investigated include porous organic polymers (POPs),[33,34] carbon-based magnetic nanocomposites,[35] silver,[36] and different polymers.[37] Although promising, these materials also have limitations, notably toxicity, precise control of surface properties and polymer size, the viability of commercial-scale production, trace-level detection, and coating concerns. Research has also focused on using 2D nanomaterials, such as $MoSe_2$, MXene, graphene, carbon nanotube, and C60 fullerenes.[38–42] However, their preparation is far from green, requiring chemical solvents and energy, leading to substantial environmental impacts.

Tris-*s*-triazine nanosheets are among the preferred 2D nanomaterials that have found a niche in environmental applications, particularly for detecting various substances in aqueous matrices.[43] Graphitic carbon nitride belongs to the graphene family and has a relatively high surface area, porosity, high density of active surface sites, earth-abundance, and few surface defects and, as such, is considered a greener alternative (non-toxic and metal-free).[44,45] However, layered nanosheets prepared from the bulk counterpart have superior properties. Due to their structural and physical properties, mechanical strength, electronic and thermal characteristics, and optical nature, they have emerged as a novel class of materials, enabling them to serve as excellent adsorbents.[46] Also, the makeup ligands in pristine g-CN (NH_2/–NH/–N) readily interact with metal ions *via* complexation by the lone pair of electrons on the nitrogen.[47]

Pioneering work on synthesizing g-CN has created a stable material for adsorbing mercury,[48] although any practical applications will require an efficient way of removing the adsorbed mercury from large sample volumes (>500 mL). A practical solution could be incorporating iron oxide into g-CN, making it magnetically retrievable. However, such an approach would necessitate a straightforward and cost-effective technique for synthesizing a magnetite/g-CN (M-g-CN) material nanocomposite with a high density of binding sites.

In this paper, we describe the development of a *de novo* strategy for preparing M-g-CN based on a thermal-assisted sonication process. The method produces an exceptionally high-affinity adsorbent material capable of efficiently capturing Hg^{2+} in various aqueous matrices with a minimum sample load of 40 mg of M-g-CN per mL. The novel synthesis method provides a high yield (97.7%) of adsorbent highly selective towards mercury ions. This study presents a proof-of-concept for utilizing M-g-CN as a highly effective adsorbent for

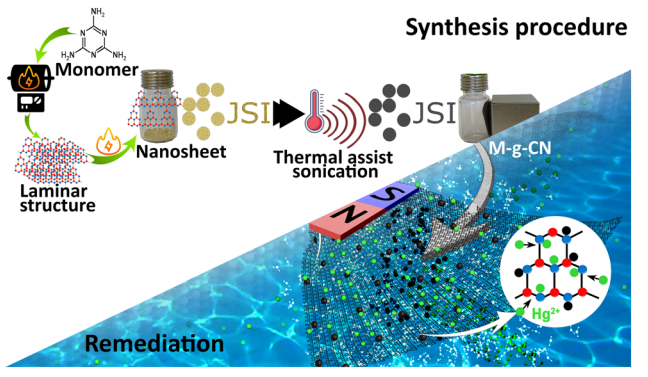

Scheme 1 Steps involved in preparing M-g-CN. Synthesis procedure: starting with a melamine monomer includes creating a bulk structure, exfoliating nanosheets with defined layers, and finally decorating the nanosheets with magnetite nanoparticles. Remediation: adsorption of Hg^{2+} with M-g-CN in aqueous media. The JSI logo indicates a change in the product's colour (yellow to black) during the synthesis process.

capturing mercury from aqueous matrices. The process for preparing and capturing mercury is illustrated in Scheme 1.

2. Material and methods

2.1. Synthesis of g-CN nanosheets from monomer

All reagents were analytical grade and obtained from Sigma-Aldrich. The synthesis protocol to prepare g-CN starts with heating melamine at 550 °C, with 6 g of melamine placed in the ceramic container and covered with another ceramic unit. The sample was then placed in a carbonite hot tube furnace with an optimized heating program: room temperature (RT) → 100 °C, at 2 °C min^{-1}, 30′, (ii) 100 °C → 350 °C, at 2 °C min^{-1}, 2 h, (iii) 350 °C → RT at 5 °C min^{-1}. The product was then placed in a mortar and ground to a powder. The powdered sample was then placed back in the oven with further heating: (i) RT → 100 °C, at 2 °C min^{-1}, 30′, (ii) 100 °C → 590 °C, at 2 °C min^{-1}, held 4 h, (iii) 590 °C → RT, at 5 °C min^{-1}. To prepare the g-CN nanosheets, 1 g of the above-prepared powder was dissolved in 25 mL of 10 M HCl solution and mixed for 4 h at RT. The solution was then filtered (0.45 μm) and dried overnight at 105 °C. Next, 100 mg of the dried sample was dispersed in 200 mL of ultra-pure water by sonicating the solution for 2 h at RT. The sample was centrifuged at 3000 rpm for 15 min. The supernatant was carefully removed, and the suspension was transferred to a clean flask. After removing the water by distillation or using a rota evaporator, the product was dried overnight at 105 °C.

2.2. Fabrication of tris-*s*-triazine carbon nitride nanosheet decorated magnetite nanoparticles

Magnetite-decorated nanosheets were prepared according to the methods reported in the literature and incorporated a modified sonication step to create a uniform distribution of magnetite on the surface of the nanosheets.[49–51] This method produces a high yield of M-g-CN (97.7%) with minimum loss compared with other synthetic methods. The method involved mixing the $FeCl_3{\cdot}6H_2O$ in a polymer blend using ultrasound nebulization for 10 min at 50 °C. Sodium acetate powder was added, and the mixture was sonicated for 10 min at 50 °C in 70% hexamethylenediamine (HMDA). The solution was then further sonicated for 30 min at 60 °C. The as-synthesized g-CN was added, and the mixture was further sonicated for 3 h at 60 °C. The solution was transferred to a Teflon vial and autoclaved (hydrothermal process) at 175 °C for 7 h. The solution was then allowed to cool at RT, centrifuged at 10 000 rpm for 10 min with rinsing using deionized water (3×) and absolute ethanol (3×) and collected by external magnetism. The solution was then dried overnight at 80 °C. The final black-coloured product was stored in an air-tight container.

2.3. Characterization of materials

The as-prepared samples (g-CN and M-g-CN) were analyzed using Fourier transform infrared spectroscopy (FTIR), Bruker IFS 66/S. X-ray diffraction (XRD) spectra of powdered samples were obtained according to standard procedure and recorded using a high-resolution XRD diffractometer (Malvern Panalyticalal X'Pert3) at a wavelength of $CuK\alpha_1$ = 1.5407 Å. Morphological features of the materials were examined using scanning electron microscopy (SEM), tunnlelling electron microscopy (TEM – Joel), and atomic resolution scanning transmission electron microscopy (STEM, ARM 200 CF). Atomic force microscopy (AFM, Witec alpha 300) was used to calculate the thickness profile and height of the nanosheets. In addition, the WITec alpha 300 microscope, which enables single spectra and Raman image measurements, was used to determine the nanosheets chemical structure.

X-ray photoelectron spectroscopy (XPS, Physical Electronics Inc., model TFA) was used to study the material's chemical configuration and elemental makeup. During experiments, the XPS chamber pressure was maintained at 6 × 10^{-8} Pa. The target (200 to 300 mm^2) was excited using a monochromatic source ($AlK\alpha_{1.2}$) at 1487.6 eV. Photoelectrons released during the process were determined at 45° normal to the surface. The energy used for resolution was set to 0.5 eV with 187.84 eV pass energy to acquire the survey scan of the samples. The C1 spectra were recorded with 29.34 eV pass energy and 0.124 eV pulse energy step, and the XPS spectra were recorded and analyzed with MultiPak v 8.1 software, Physical Electronics, Japan.

Standard symmetrical Shirley background subtraction was used for spectra fitting using the Gauss–Lorentz-based function. The surface area, pore size, and nitrogen adsorption were recorded using Brunauer–Emmett–Teller analysis, (BET), Micromeritics Instrument Corp.

All solid-state NMR experiments were conducted using an Agilent Technologies NMR System 600 MHz NMR spectrometer with a 3.2 mm NB Double Resonance HX MAS Solids Probe. Cross-polarization (CP) and magic-angle spinning (MAS) techniques were employed for ^{13}C and ^{15}N experiments, with high-power proton decoupling during acquisition. Spectra were recorded at a spinning rate of 16 kHz for ^{13}C measurements and 10 kHz for ^{15}N measurements. Chemical shifts for ^{13}C and ^{15}N were referenced to tetramethylsilane and nitromethane, respectively.

2.4. Production of the ^{197}Hg radiotracer

Mercury, enriched with 51% ^{196}Hg, was procured from Isoflex (San Francisco, USA). The use of ^{197}Hg radiotracer eliminates the risk of sample contamination. Acidified enriched ^{196}Hg was placed in a quartz ampoule, sealed, and irradiated for 20 h in the reactor core central channel (250 kW) of a TRIGA Mark II research reactor (Fig. S1, ESI†). The ^{197}Hg radiotracer was produced in the reactor core using a high flux of neutrons (10^{13} n cm^{-2} s^{-1}). Before irradiation, the concentration of Hg in the solution was calculated using Hg-201 (Sanso Seisakusho Co., LTD). A concentration of 100 μg mL^{-1} was used as a reference. The Hg solution was appropriately diluted to the required concentrations to study

nanomaterial binding. The detailed Experimental procedures and determination of ^{197}Hg using a gamma detector for the testing and binding efficiencies of M-g-CN are provided in the ESI.†

2.5. Procedure for testing the binding efficiency of M-g-CN

2.5.1. Experimental procedure. A magnetic nanomaterial (40 mg) sample was weighed into a clean and dry 10 mL Teflon centrifuge vial. Then 3 mL of 75 pg mL^{-1} $^{197}Hg^{2+}$ solution (neutral pH, MQ water) was added. The centrifuge vial was then shaken for 1 h. After shaking, the precipitate was separated from the supernatant using a neodymium magnet (N35/Ni; magnetic induction 0.5 T). Two mL of supernatant were transferred into a vial and diluted to 8 mL with MQ water. The remaining supernatant (1 mL) was mixed with concentrated HCl (3 mL) to leach $^{197}Hg^{2+}$. After 20 minutes, the supernatant was centrifuged at 3200 RPM for 5 min. The leftover supernatant (1 mL) was removed, and concentrated HCl acid (3 mL) was added again following the previous procedure. Three measurement vials were obtained: (1) supernatant, (2) first acid precipitate, and (3) second acid precipitate. The samples and the remaining $^{197}Hg^{2+}$ were then measured using a gamma well detector (section 2.5.2).

Scheme 2 demonstrates the purpose of acid leaching instead of directly measuring the precipitate. Acid leaching resulted in a lower apparent activity than measuring the precipitate since more gamma and X-rays can escape from the detector due to the different sample geometries. Also, standards for gamma well measurements can be obtained only in solution, not precipitation.

Since the activity of the leftover $^{197}Hg^{2+}$ in the precipitate after double leaching was minimal (<1% of the activity obtained before leaching), the measurement error originating from the above-described geometry discrepancy is small and can therefore be neglected.

2.5.2. Determination of ^{197}Hg using gamma detector. Standards preparation for gamma detector experiments were in triplicate with a total volume of 8 mL containing 2% HNO_3 and later shifted to the vials for measurements. In order to be consistent within the measured activity of the samples, standard solutions should dilute every time prior to the analysis. The X-rays and γ-rays activities in the standard solutions were in vials analyzed using an HPGe detector with high germanium purity.

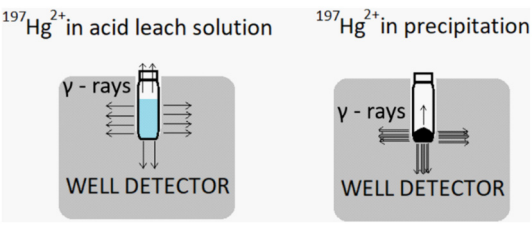

Scheme 2 Schematic illustrations of $^{197}Hg^{2+}$ in acid leach and precipitation measurement, the effect of different geometries on the activity measurement.

Peak areas were used to determine the concentration of ^{197}Hg in the samples by comparing X and γ-ray emissions in the form of two doublet peaks at 67.0 and 77.3 (68.8 keV and 77.9 keV). The activities obtained during the analysis were recalculated based on the reference time using eqn (1), derived from the law for radioactive decay (exponential) of the substrate. Eqn (1) was used to calculate both the activity (A_0) of the reference time of the sample and the standard. The mercury recovery from the M-g-CN nanocomposite was calculated according to eqn (2).

$$A_{0,\text{sample}} = \frac{A_{\text{sample}} \times \frac{\ln 2}{t_{\frac{1}{2}}}}{e^{-\left(\frac{t_{\text{passed}} \times \ln 2}{t_{\frac{1}{2}}}\right)} \times \left[1 - e^{-\left(\frac{t_{\text{measurement}} \times \ln 2}{t_{\frac{1}{2}}}\right)}\right]} \quad (1)$$

$$R = \frac{A_{0,\text{sample}}}{A_{0,\text{std.}}} \times \frac{m_{\text{Hg,std.}}}{m_{\text{Hg,sample}}} \times f_{\text{dillution}} \times 100 \quad (2)$$

where:
A_0 = activity of sample t = 0 [Bq]
A_0 = activity at reference time t = 0 [Bq]
A_{sample} = activity of sample during analysis [Bq]
$t_{\frac{1}{2}}$ = half-life (^{197}Hg) [s],
t_{passed} = interval between t = 0 and the start of the measurement [s]
$t_{\text{measurement}}$ = time passed during the measurement [s]
R = recovery [%]
$m_{\text{Hg,std.}}$ = mass of Hg in standard solutions [pg]
$m_{\text{Hg, sample}}$ = mass of Hg in the sample, assuming 100% recovery [pg]
$f_{\text{dillution}}$ = dilution factor.

3. Results and discussion

3.1. Material synthesis and chemical properties

A densely packed distribution of magnetite on g-CN nanosheets was obtained using a series of thermal and sonication steps to produce M-g-CN in a high yield (97.7%). FTIR and XRD were used to study the signature details of g-CN and an impregnated M-g-CN nanocomposite decorated with Fe ions. The FTIR spectrum shows broad peaks between 3240–3500 cm^{-1} with N–H/O–H bonds characteristic of its stretching vibration (Fig. 1a).[52] The peak at 806 cm^{-1} was assigned to the tris-*s*-triazine heptazine ring and showed a characteristic bending out-of-plane vibration,[48] whereas peaks between 1147 and 1632 cm^{-1} have signatures characteristics of *s*-triazine by-products.[53] The spectrum of M-g-CN has similarities with g-CN except for a peak at 564.7 cm^{-1}, which relates to Fe–O stretching (Fig. 1a).[54] XRD analysis of the M-g-CN crystalline structure revealed peaks at 2θ = 12.8° and 27.26° resembling the structural features of tris-triazine interplanar units (001) and aromatic system (002), respectively (Fig. 1b).

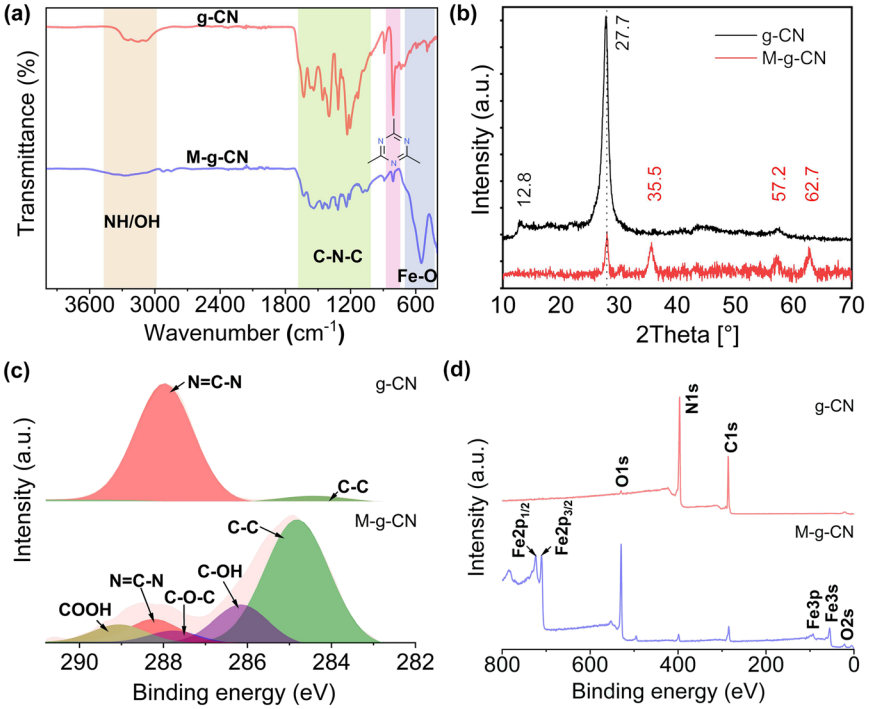

Fig. 1 Crystalline and phase studies of as-synthesized g-CN and M-g-CN (a) FT-IR spectra showing different functionalities of the samples with distinct characteristics. (b) XRD pattern of samples. (c) High-resolution C1 spectra. (d) Survey profile with an arrangement of elements.

The XRD pattern of the M-g-CN reveals peaks with different indices (220), (311), (400), (422), (511), and (440), which are best aligned with the magnetized particles (Fig. 1b).[55,56] The M-g-CN spectra exhibit a distinctive peak corresponding to the graphitic backbone of g-CN, indicating the successful loading of magnetite on the nanosheets. This observation is consistent with the findings of Kim *et al.*,[56] who demonstrated that the sonochemical method results in a spinel magnetite crystal structure.

To further assess the structural integrity and chemical species associated with their structures, Raman and XPS profiles were obtained to confirm the preservation of the transformed M-g-CN. As depicted (Fig. S2a, ESI†), the D and G bands of g-CN are at 1358 cm^{-1} and 1594 cm^{-1}, which represents A_{1g} of the sp^3 carbon atom of disordering graphitic nature with in-plane vibration of sp^2 carbon atom, and E_{2g} vibration with *k*, showing that the sample is amorphous.[57] However, the graphitic carbon nitride structure is more complex than graphene, and obtaining signals from the triazine-based structure is challenging. Therefore, Raman mapping was performed at different regions of the g-CN nanosheets with defined thicknesses to integrate D and G peaks. Contrary to g-CN, M-g-CN shows characteristic bands at 214, 279, 379, 483, and 583 cm^{-1} corresponding to magnetite,[58] while a flattened peak at 1267 cm^{-1} resulted from the unique characteristics of C–N, *i.e.*, the successful arrangement of magnetite on the g-CN nanosheets. The intensities of D and G bands are very low and barely visible in the M-g-CN spectra because of magnetite's anchoring and masking effect over the surface of the g-CN (Fig. S2a, ESI†).

The surface chemical compositions of g-CN and M-g-CN were further investigated using XPS (Fig. 1c and d and S2b, ESI†). The deconvoluted C1s, N1s, and survey XPS spectra of g-CN and M-g-CN are shown in Fig. 1c and d and S2b, ESI.† They reveal almost identical surface chemistries, except for some functional groups present on M-g-CN due to the involvement of cross-linking agents during synthesis. The C1s spectrum peaks in the samples were deconvoluted at 284.91 and 288.32 eV, resulting from graphitic surface adventitious carbon (C–C) and sp^2 carbon in tri-*s*-triazine (N=C–N), respectively.[59] The N1s spectra are deconvoluted to peaks at 398.4 eV, 399.8 eV, and 400 eV (Fig. S2a, ESI†). The peak at 398.6 eV relates to the sp^2–N in triazine (N=C–N); however, a second peak at 400.1 eV can be ascribed to a tertiary N in N–$(C)_3$/N bonded to H. The presence of functional moieties (C–NH) is confirmed by the peak at 401.1 eV, which generates from the aromatic melon structure of triazine as imperfect condensation. It was also shown that the tri-*s*-triazine units are interconnected with amino groups between the sheets.[48] Survey spectra of the samples pertain to the availability of carbon (C), nitrogen (N), oxygen (O), and iron (Fe) peaks (Fig. 1d), with two peaks for M-g-CN that correspond to Fe $2p_{1/2}$ (723.5 eV) and Fe $2p_{3/2}$ (710.0 eV).[58]

3.2. Spatial distribution topographies and molecular structure analysis

The nanosheet height profile and thickness associated with the as-synthesized g-CN (Fig. 2a and b) were performed using atomic force microscopy (AFM). The nanosheets are highly

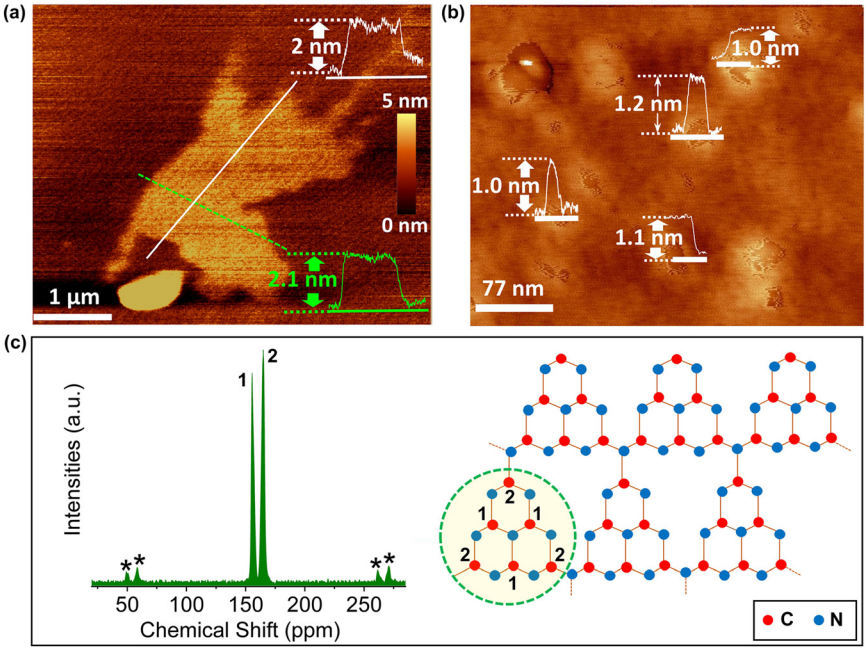

Fig. 2 (a) AFM image of g-CN nanosheet with sectional profile measurement showing height and thickness profiles (nm). (b) AFM images of nanosheets with respective height profiles at different locations. (c) Solid-state ^{13}C NMR spectra of as-prepared g-CN and its idealized structure showing heptazine tectonic units.

concentrated and dispersed in the sample with an average thickness obtained from three AFM image cross-sections of about 1.0, 1.1 and 1.2 nm (Fig. 2b), corresponding to approximately 2–4 layers. The g-CN nanosheets have an average thickness of about 1.1 nm.[60]

Statistical studies on the thickness of g-CN nanosheets by measuring different places confirm this observation (Fig. 2a and b). Further, the structure of tris-*s*-triazine was studied using ^{13}C cross-polarization magic-angle spinning (CP-MAS) NMR to identify the integrity of the chemical structure.[61,62] It can be seen that the sample, two peaks at 155.52 and 164.96 ppm correspond to the C_1 of N=C–N_2 and C_2 of N=C–N(NH_x) in heptazine structure in the corrugated g-CN melon networks, respectively, and the black asterisks denote spinning sidebands (Fig. 2c).[63,64] These assignments agree with g-CN ^{13}C NMR,[65] further indicating that the g-CN nanosheets comprise heptazine tectonic units of the solid-state NMR spectra.

3.3. Morphological studies

High-resolution transmission electron microscopy (HRTEM) was used to examine the morphological and microstructural integrity of g-CN and M-g-CN. Comparative images of bare magnetite, g-CN nanosheets, and M-g-CN, along with their corresponding selected area electron diffraction (SAED) patterns, were analyzed in detail (Fig. 3). The resultant images show how the magnetite nanoparticles arranged on the TEM grids are visible as clusters, irregularly faceted and floccules. (Fig. 3a–d). The particles are distributed evenly with maintained spherical morphology. The TEM images of g-CN indicate well-distributed slices arranged in a pile of blanket sheath stacking on the surface like randomly oriented graphene-like layers, which are relatively smooth in appearance (Fig. 3e–g). Few layered g-CN nanosheets with flat surfaces visible with peculiar transparent sheet-like appearance and layered bundles on the TEM grids (Fig. 3f and g). The selected area in the HR-TEM image (Fig. 3h) displays a complete diffraction ring corresponding to the representative (001) plane of g-CN. It was observed as six dots from the fast Fourier transform (FFT) image (Fig. 3h, inset image), which resembles g-CN triazine layers. As indicated in the TEM image of M-g-CN (Fig. 3i and j), the well-defined magnetite is randomly anchored on the surface of g-CN, and no hard aggregation was observed without free nanoparticles outside the g-CN nanosheet, which prevents the possible agglomeration of magnetite nanoparticles.[66] This fact allows the nanosheets to serve as a substrate for the attachment/growth of magnetite particles.

Moreover, an average diameter of 15.5 nm with an interplanar distance of d = 0.27 nm and 0.50 nm (Fig. 3k) indicates the presence of (311) and (111) planes of magnetite crystals.[66–68] The SAED pattern confirms that M-g-CN has better stability and crystallinity than bare g-CN, mainly because of the anchoring of the magnetite particles on the g-CN nanosheet surfaces, indicating the presence of magnetite (Fig. 3l). The ring patterns observed in SAED are indexed to the (220), (311), (400), (422), (511), (440), and (553) planes of magnetite, which is in agreement with the XRD spectra.[69] The SAED patterns exhibit diffraction spots and rings simultaneously, implying long-range ordering of nanocrystals on the surface of g-CN. The appearance of an additional plane indexed of 002, equivalent to a *d*-spacing of

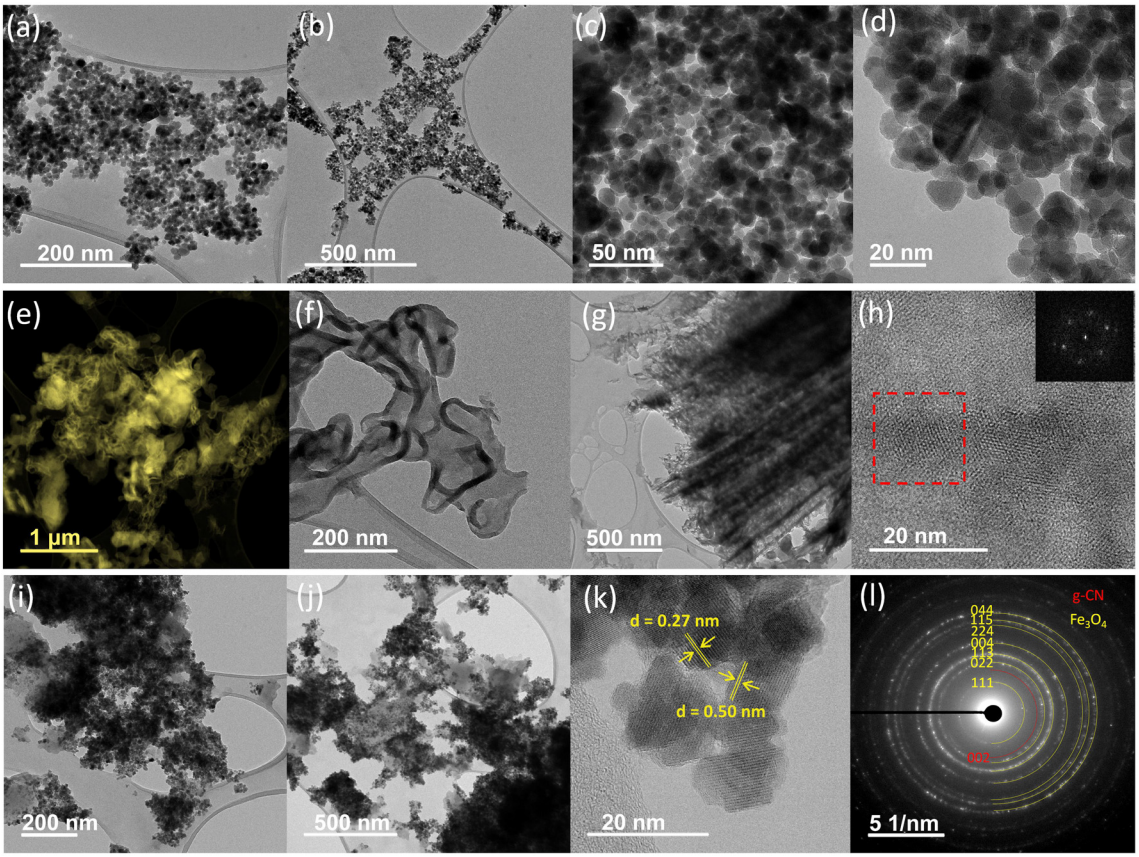

Fig. 3 TEM and HRTEM images of Fe_3O_4 were obtained at different magnifications (a–d), g-CN images showing nanosheets morphologies (e–h) and M-g-CN (i–l). (e) Intercalated g-CN structure (f and g) layered g-CN nanosheet. (h) HRTEM image of g-CN with inset image showing a typical FFT pattern of triazine layers of g-CN. (i and j) TEM images of M-g-CN nanocomposite. (k) The interplanar lattice spacing for Fe_2O_3 in M-g-CN nanocomposite. (l) SAED pattern of M-g-CN with concentric line patterns.

0.234 nm of g-CN, in the HR-TEM image (Fig. 3l) is attributed to the distance between the layers of the graphitic nanosheets.[70] This proves the heterostructure of the M-g-CN, where the g-CN nanosheet serves as a template to accommodate magnetite nanoparticles in the resulting nanocomposite.

3.4. Elemental analysis studies of M-g-CN

Elemental mapping was further utilized to examine the formation of M-g-CN with desired and available element compositions (Fig. 4a and b) using scanning electron microscopy (SEM) combined with energy-dispersive spectroscopy (EDS). The oxygen that appeared in the sample (marked blue in the EDS mapping images) likely arises from oxygen functionalization or moisture on the surface of the g-CN due to using an open muffle furnace.[71] Besides oxygen, an even distribution of C (purple), N (green), and Fe (red) is evident in the EDS colour map (Fig. 4a). Fig. 4b shows a typical EDS spectrum of the M-g-CN nanostructure material. The significant peaks observed around 0.61, 6.30, and 7.1 keV represent iron (Fe) and oxygen (O) energies, confirming the strong anchoring of the magnetite particles on the g-CN surfaces.[72] The percentage composition of the four elements of C, N, O, and Fe is 19.62 wt%, 9.96 wt%, 22.27 wt% and 48.15 wt%, respectively. In brief, the images of EDS and mapping are consistent with the XRD, FTIR, and XPS results that support the evidence of assembly.

3.5. Investigation of g-CN and M-g-CN surface area and binding properties

Before performing Hg^{2+} adsorption studies, the adsorption and surface area properties were defined. Pore size distributions of as-prepared materials were investigated using Barrett–Joyner–Halenda (BJH) analysis (Fig. 5a). The BJH shows a broad peak near the 0–35 nm range as a result of irregular pores generated from the confined voids in the g-CN nanosheets. The BET surface area was calculated over a range of relative pressures (P/P_0). The BET plots (Fig. 5b and c) of g-CN and M-g-CN, with the resulting surface area of g-CN and M-g-CN being ~19.5 and ~96.8 $m^2\ g^{-1}$, respectively. This difference is due to the accumulation of Fe nanoparticles on the surface of g-CN. Adsorption–desorption examination of g-CN and M-g-CN display type-IV isotherms with hysteresis-III (Fig. 5b). The microporous properties and large surface area favour more binding/active sites accessible to M-g-CN.

Experiments were also performed to analyze the constraint of M-g-CN towards trace levels of Hg^{2+} from different

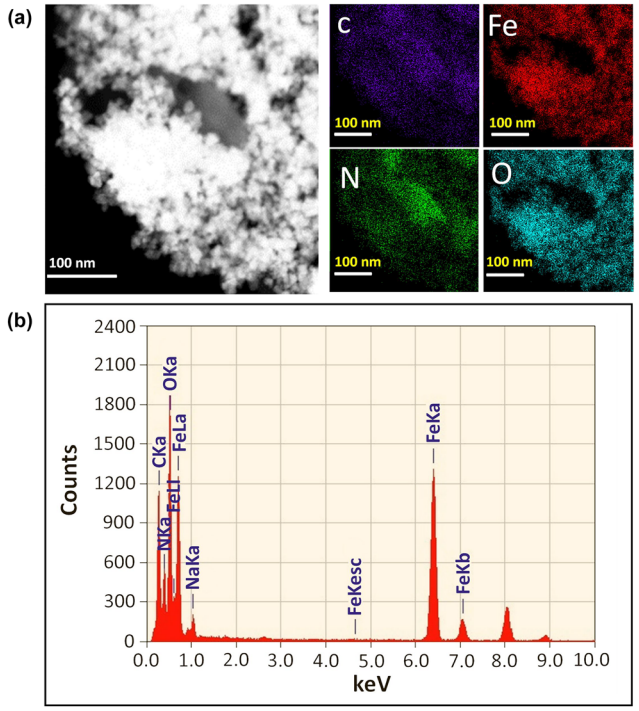

Fig. 4 (a) SEM and EDS elemental mapping of C, Fe, N, and O of M-g-CN. (b) EDX spectra of M-g-CN nanocomposite with element arrangements.

matrices. These experiments allowed M-g-CN to adsorb Hg^{2+} at its near-natural environmental concentrations. For this purpose, a ^{197}Hg radioactive isotope was used, and analysis was performed using well-type high-purity germanium (HPGe) detector. The binding mechanism of Hg^{2+} (natural abundance standard solution) on g-CN and M-g-CN was investigated using the XPS (Fig. 5d and S3, ESI†). Using ^{197}Hg radiotracer in the present study has benefits over conventional Hg analysis regarding uncertainties due to Hg carryover and blank measurements. This is not the case with ^{197}Hg radiotracer, as the Hg isotope is absent naturally. Hence, the analytical problems and uncertainties at natural Hg levels are minimized using ^{197}Hg.[73]

The main Hg4f peak, a doublet representing spin-orbit splitting of about 4 eV for the $Hg4f_{7/2}$ and $Hg4f_{5/2}$ states, was observed at a binding energy of about 100.2 and 104.2 eV, respectively, and found in the oxidizing state of mercury (Hg^{2+}).[74] Besides the peaks originating from Hg^{2+} binding, two more peaks appear with binding energies of 710.1 and 723.6 eV, corresponding to Fe-$2p_{3/2}$ and Fe-$2p_{1/2}$, respectively, characteristic of magnetite (Fig. 5d).[75] These results confirmed the successful adsorption of Hg^{2+}.

After the adsorption of Hg^{2+} (Fig. S3, ESI†), the shift in binding energies of C 1s, N 1s, O 1s, and Fe 2p XPS spectra of g-CN and M-g-CN is not statistically significant, likely arise

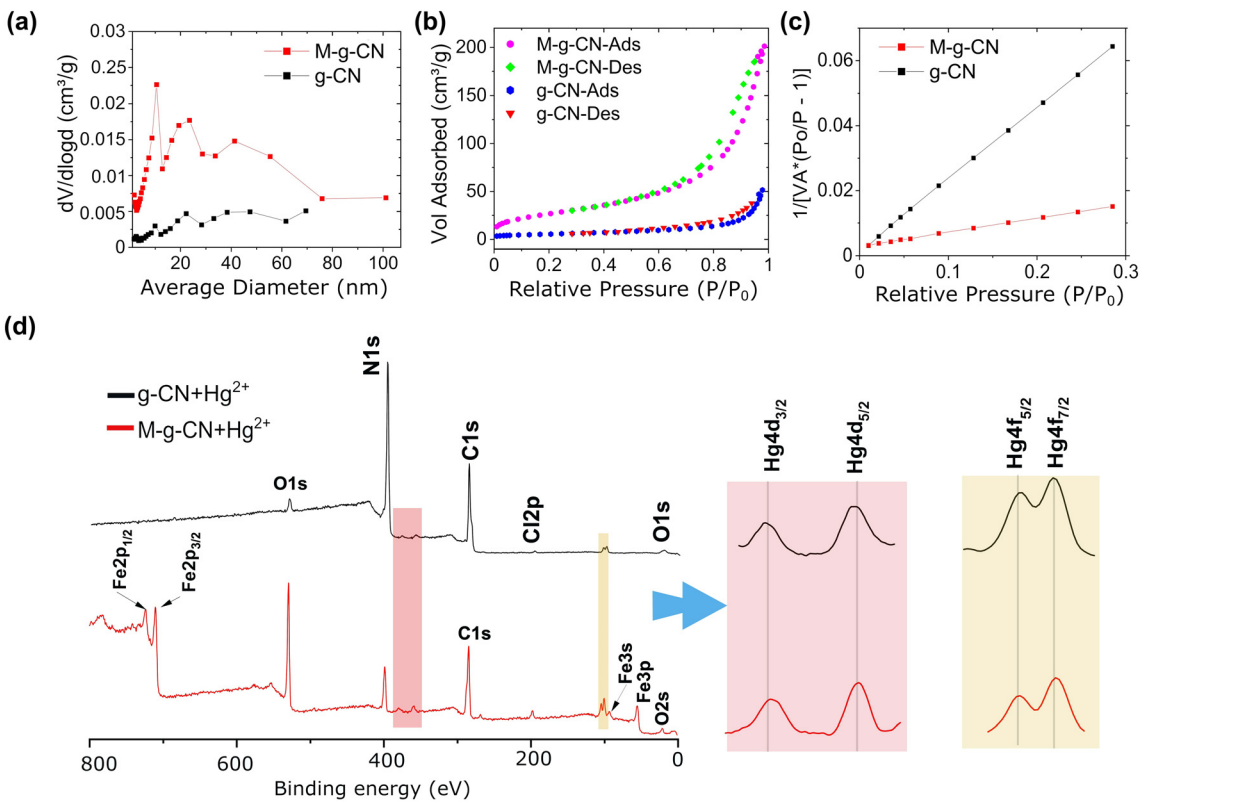

Fig. 5 (a) BJH plot with pore size distribution curve of g-CN and M-g-CN respectively. (b and c) The BET surface area of g-CN nanosheets and M-g-CN nanocomposite (d) survey spectra profile depicting Hg^{2+} binding regions. The two doublet peaks of Hg4f ($Hg4f_{7/2}$ and $Hg4f_{5/2}$) and Hg4d ($Hg4d_{5/2}$ and $Hg4d_{3/2}$) are highlighted in pink and yellow, respectively, showing the direct binding of Hg^{2+} to the g-CN surface rather than on bare Fe nanoparticles.

as a result of charging effects. Another explanation is that the change in the local bonding environment does not cause significant shift. It should also be noted that the amount of adsorbed Hg is only about 0.5 at%, insufficient to cause a noticeable shifts in the binding energy. According to the literature, reported shifts are in the order of 0.1 eV.[76] However, in our case, this could not be confirmed.

Prior to Hg adsorption (Table S1†), the M-g-CN sample contained significant amounts of elemental Fe, O, C and N elements. After Hg^{2+} adsorption, the amount of Fe and O is reduced, while the amount of C and N doubles. The reason for this is likely rearrangement during the adsorption of Hg^{2+}. Since XPS is a surface sensitive technique, it can be concluded that more g-CN components should be present at the surface, so also Hg^{2+} should interact with N–H and C≡N groups and not with Fe_2O_3. This observation agrees with data from other studies investigating the interaction of Hg^{2+} with Fe_3O_4 that reported no or negligible binding.[36,77–81]

3.6. Binding coordination studies with ^{13}C and ^{15}N NMR

A detailed study of the binding constraints of Hg^{2+} with the material was analyzed with ^{13}C and ^{15}N. The results revealed that Hg^{2+} binds to the heptazine structure of g-CN and not the magnetite particles (Fig. S4–S6, ESI†). The Hg^{2+} receives electrons to form coordination centers not restricted to the specific atomic environments but distributed about the triazine structure. With this, Hg^{2+} ions are organized in the spaces with reciprocal points to lines, significantly recovering the space consumed and increasing the adsorption volume for M-g-CN (Table S1, ESI†). The acquisition time to carry out ^{13}C was 0.03 s with repetition delays of 7 s. The number of scans was 1592 for g-CN and 8656 for g-CN + Hg^{2+}. For ^{15}N experiments, acquisition time was 0.021 s with repetition delays of 7 s. The number of scans was 13 008 for g-CN and 12 136 for g-CN + Hg^{2+}.

3.7. Binding efficiency studies of M-g-CN

To check the binding efficiencies of as-produced M-g-CN to adsorbed Hg^{2+}, different pH values (2–10) of the solution were selected (Fig. 6a). The results revealed that pH significantly influences the binding properties of M-g-CN with Hg^{2+}. The adsorption capacity of Hg^{2+} by M-g-CN increases from pH 2–7 and reaches a steady state rate, and it decreases over the pH range of 7–10. The maximum binding capacity of M-g-CN for Hg^{2+} was observed at pH 7; hence, this value was considered optimal and ideal for further investigations.

A possible effect of pH on Hg^{2+} adsorption can be postulated by the adsorbent's zero-point charge (ZPC) behaviour. The pH-ZPC relation of the adsorbent material reflects the total charge on the surface of the adsorbent material.[82] When the pH of the solution is below the ZPC, the net surface charge of M-g-CN becomes positive. Due to the repulsive electrostatic forces, this makes it difficult for the Hg^{2+} to bind with the nanomaterial. However, once the pH of the solution exceeds the ZPC, the surface charge of M-g-CN becomes negative, causing Hg^{2+} ions to be attracted towards the magnetic-bound nanosheets. This attraction is due to the combined effects of the hydrating radii, functional makeup, and attractive electrostatic forces. Since the ZPC of g-CN and M-g-CN was between ≈3.8 and ≈4.7, electrostatic repulsion is observed at pH values below 4.1. In contrast, at higher pH (4.1 or more), the electrostatic repulsion changed to the electrostatic attraction (Fig. 6a). This phenomenon is due to the increase in pH, which results in an increased adsorption efficiency of Hg^{2+}, as noticed through a dramatically increased adsorption capacity (10 folds) when pH > 4.

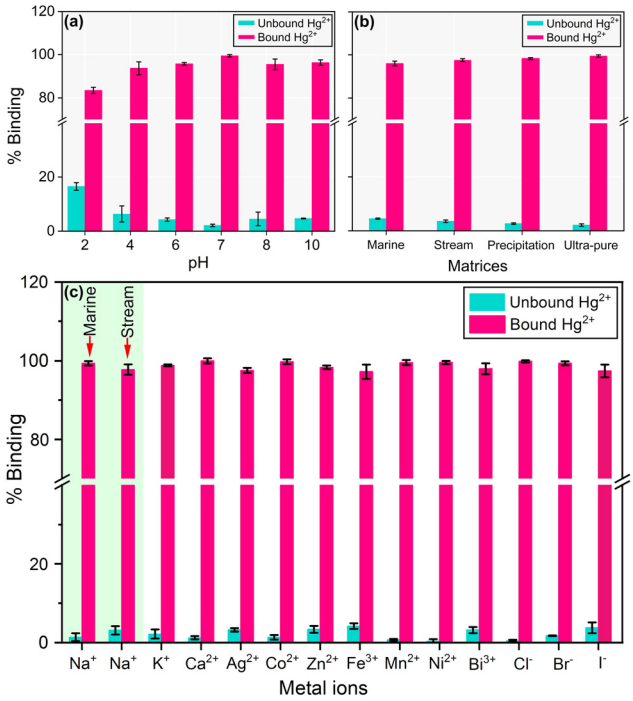

Fig. 6 Histograms of binding and performance studies of M-g-CN: (a) binding efficiencies at different pHs (pH 2–10). (b) Binding efficiencies in various aqueous matrices (marine, stream, precipitation, and ultra-pure). (c) Binding efficiency determination of Hg^{2+} towards M-g-CN in the presence of interfering ions.

In addition, a competition occurred between Hg^{2+} ion and H^+ ions towards the required sites,[83] due to increment in pH values, the competition state of binding sites reduced. Henceforth, additional adsorption sites are available to the Hg^{2+} with increased solution pH. Consequently, as the pH of the solution increases, adsorption efficiency is enhanced. The compliance effects of pH on Hg^{2+} adsorption were studied previously.[84]

The maximum binding capacity of M-g-CN (40 mg mL^{-1}) was also investigated with different concentrations of Hg^{2+} (1 to 10 000 pg mL^{-1}) and found that M-g-CN can retain 75% binding with higher concentrations (Fig. S7 and Table S2, ESI†). The adsorption of Hg^{2+} by M-g-CN with time (20, 40, 60, 80, and 100 min) was also investigated. The findings indicate that 40 min is the ideal time for maximum adsorption of Hg^{2+} (Fig. S8, ESI†).

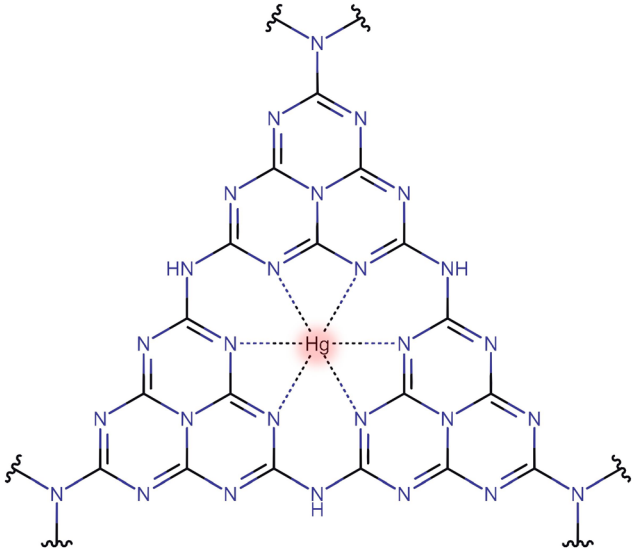

Fig. 7 Possible mechanism of interaction of Hg^{2+} with g-CN with six coordinated nitrogen atoms.

3.8. Performance evaluation of M-g-CN

In order to evaluate the efficacy of M-g-CN and assess possible interferences from other matrices, $^{197}Hg^{2+}$ was spiked into marine, stream, precipitation, and ultra-pure water at environmentally relevant concentrations (Fig. 6b, Table S3, ESI†). These results demonstrate the applicability of M-g-CN for binding mercury in various settings, from industrial effluent to natural water bodies, where M-g-CN could prevent the entry of mercury into the biosphere.

As an ideal adsorbent nanocomposite material, M-g-CN should selectively capture and remove Hg^{2+} in aqueous matrices when other potential interfering ions are present in their natural concentrations. Consequently, the affinity of M-g-CN for Hg^{2+} ions was examined based on the percent recovery when other possible interfering ions were present in the solution: Na^+, K^+, Ca^{2+}, Ag^{2+}, Co^{2+}, Zn^{2+}, Fe^{3+}, Mn^{2+}, Ni^{2+}, Bi^{3+}, Cl^-, Br^- and I^- (Fig. 6c, Table S4, ESI†). It was worth noting that M-g-CN can capture Hg^{2+} efficiently with maximum recovery with all the interfering ions in the solution.

Furthermore, by only heating the sample, M-g-CN could be fully regenerated due to the stability of the tris-s-triazine framework and nanostructure chemical stability, which remains essential for extended usage. Under elevated temperature, the adsorbed Hg^{2+} is thermally reduced to Hg^0, desorbed from the M-g-CN surface, and swept away. The adsorption efficiency of M-g-CN drops to 8.3% after nine repeated trials. After ten rounds, Hg^{2+} absorbance decreased by ≤20% (Fig. S9, Table S5, ESI†).

Fig. 7 shows a possible mechanism of interaction of Hg^{2+} on the surface of g-CN. The Hg^{2+} interacts with six nitrogen lone pair electrons to form complex and potential binding sites. This observation is well supported by the ^{13}C and ^{15}N CP-MAS NMR spectra (S4–S6, ESI†).

4. Conclusions

The work demonstrated a new "green" innovative concept for preparing M-g-CN nanocomposite based on thermally triggered intermittent sonication for capturing Hg^{2+} in environmental remediation and industrial applications. The developed synthesis method provides a high yield (97.7%) and relatively large surface area (96.8 m^2 g^{-1}) of M-g-CN. The M-g-CN has high Hg^{2+} binding capacities for Hg^{2+} at trace levels in natural aqueous matrices compared with other nano adsorbents such as activated charcoal, metal oxides, nanocomposites and nanostructure materials. M-g-CN was stable under different pH conditions and selective towards Hg^{2+} under the influence of other potential interfering ions. In addition, a combination of highly adsorbing nanosheets and the magnetic properties of the magnetite serve the purpose of concentrating and efficiently recovering Hg^{2+}. Notably, a simple heating procedure allows the M-g-CN to be fully regenerated (10 repeated cycles) due to the thermal and chemical stability of the tris-*s*-triazine and nanostructured framework, adding to its potential cost-effectiveness and sustainable use. The as-synthesised magnetic has many potential applications besides those discussed, such as passive sampling for use onboard ships for monitoring global ocean mercury (and other potentially toxic elements) levels. Significantly, it can outpace conventional adsorbents and traps, which are expensive, require skilled personnel, and have much lower binding efficiency. The results obtained from this study affirm the efficacy of M-g-CN as an exceptional adsorbent material for capturing transition metals across various applications, ranging from wastewater treatment to passive sampling materials.

Author contributions

Raghuraj Singh Chouhan: methodology, investigation, conceptualization, writing-original draft, writing, reviewing and editing, visualization, software, and funding acquisition. Jan Gačnik: experimental analysis on radiotracer, writing, reviewing and editing, visualization, and data curation. Igor Živković: writing, reviewing and editing, visualization, investigation. Sreekanth Vijayakumaran Nair: graphical and figure design, editing. Nigel Van de Velde: experimental analysis, visualization on AFM. Alenka Vesel: experimental analysis on XPS. Primož Šket: experimental analysis on NMR. Sonu Gandhi: writing, reviewing, and editing. Ivan Jerman: writing, reviewing, and editing. Milena Horvat: conceptualization, reviewing and editing, visualization, and funding acquisition.

Conflicts of interest

There are no conflicts to declare.

Acknowledgements

We gratefully acknowledge the MercOx project (Metrology for oxidized mercury; 16ENV01) funded under EMPIR (The

European Metrology Programme for Innovation and Research). The H2020 ERA-NET Cofund, GA 689443 ERA-PLANET/IGOSP, has also supported the work. The Slovenian Research Agency is acknowledged through funding projects ARRS N1-0100, J1-1716, P2-0393, BI-US/22-24-162, IsoCont J1-3033, P1-0143 and P1-0242.

References

1 M. Jakob, J. C. Steckel, F. Jotzo, B. K. Sovacool, L. Cornelsen, R. Chandra, O. Edenhofer, C. Holden, A. Löschel, T. Nace, N. Robins, J. Suedekum and J. Urpelainen, The future of coal in a carbon-constrained climate, *Nat. Clim. Change*, 2020, **10**, 704–707.

2 Mandeep, G. Kumar Gupta and P. Shukla, *Bioresour. Technol.*, 2020, **297**, 122496.

3 T. W. Clarkson, The three modern faces of mercury, *Environ. Health Perspect.*, 2002, **110**, 11–23.

4 N. Pirrone, S. Cinnirella, X. Feng, R. B. Finkelman, H. R. Friedli, J. Leaner, R. Mason, A. B. Mukherjee, G. B. Stracher, D. G. Streets and K. Telmer, Global mercury emissions to the atmosphere from anthropogenic and natural sources, *Atmos. Chem. Phys.*, 2010, **10**, 5951–5964.

5 G. Charbonnier, C. Morales, S. Duchamp-Alphonse, S. Westermann, T. Adatte and K. B. Föllmi, Mercury enrichment indicates volcanic triggering of Valanginian environmental change, *Sci. Rep.*, 2017, **7**, 40808.

6 UN Environment, *Global Mercury Assessment 2018. UN Environment Programme, Chemicals*, 2019.

7 S. N. Lyman, D. A. Jaffe and M. S. Gustin, Release of mercury halides from KCl denuders in the presence of ozone, *Atmos. Chem. Phys.*, 2010, **10**, 8197–8204.

8 L. Zhang, S. Wang, Y. Meng and J. Hao, Influence of Mercury and Chlorine Content of Coal on Mercury Emissions from Coal-Fired Power Plants in China, *Environ. Sci. Technol.*, 2012, **46**, 6385–6392.

9 Z. Ramezani, N. Pourmand, A. Behfar and A. Momeni, Removal and recovery of mercury from chlor-alkali petrochemical wastes using γ-Fe2O3 nanoparticles, *Appl. Petrochem. Res.*, 2016, **6**, 403–411.

10 D. Evers, in *Encyclopedia of the Anthropocene*, Elsevier, 2018, pp. 181–194.

11 M. A. Coulter, Minamata Convention on Mercury, *Int. Leg. Mater.*, 2016, **55**, 582–616.

12 F. S. A. Khan, N. M. Mubarak, Y. H. Tan, R. R. Karri, M. Khalid, R. Walvekar, E. C. Abdullah, S. A. Mazari and S. Nizamuddin, *Environ. Sci. Pollut. Res.*, 2020, **27**(19), 24342–24356.

13 Y. Wang, T. Xu, E. Song, Z. Wang, H. Cheng, Z. Ma, Y. Bian, Y. Hu, F. Wang, Y. Song, C. Gu, X. Yang, M. Ye, F. Orori Kengara and X. Jiang, Mercury adsorption and reduction by nonlinear optical material (NLOM) DMABR loaded on Sepiolite: A mechanism study, *Chem. Eng. J.*, 2023, **453**, 139787.

14 W. Liu, X. Zhao, T. Wang, J. Fu and J. Ni, Selective and irreversible adsorption of mercury(II) from aqueous solution by a flower-like titanate nanomaterial, *J. Mater. Chem. A*, 2015, **3**, 17676–17684.

15 D. Wang, A. Mukhtar, M. Humayun, K. Wu, Z. Du, S. Wang and Y. Zhang, A Critical Review on Nanowire-Motors: Design, Mechanism and Applications, *Chem. Rec.*, 2022, **22**, e202200016.

16 D. S. Wang, A. Mukhtar, K. M. Wu, L. Gu and X. Cao, *Materials*, 2019, 12.

17 G. H. Qasim, S. Lee, W. Lee and S. Han, Reduction and removal of aqueous Hg(II) using indium-modified zero-valent iron particles, *Appl. Catal., B*, 2020, **277**, 119198.

18 S. De Gisi, G. Lofrano, M. Grassi and M. Notarnicola, Characteristics and adsorption capacities of low-cost sorbents for wastewater treatment: A review, *Sustainable Mater. Technol.*, 2016, **9**, 10–40.

19 S. Kalia, S. Kango, A. Kumar, Y. Haldorai, B. Kumari and R. Kumar, Magnetic polymer nanocomposites for environmental and biomedical applications, *Colloid Polym. Sci.*, 2014, **292**, 2025–2052.

20 J. Li, X. Wang, G. Zhao, C. Chen, Z. Chai, A. Alsaedi, T. Hayat and X. Wang, Metal-organic framework-based materials: superior adsorbents for the capture of toxic and radioactive metal ions, *Chem. Soc. Rev.*, 2018, **47**, 2322–2356.

21 D. Wang, Y. Hu, Z. Cui, P. X. Yang, Z. Du, Y. Hou, P. Yang, J. Rao, C. Wang and Y. Zhang, Sulfur vacancy regulation and multipolarization of NixCo1S nanowires-decorated biotemplated structures to promote microwave absorption, *J. Colloid Interface Sci.*, 2023, **646**, 991–1001.

22 D. Wang, P. Yang, Y. Hu, Z. Cui, Z. Du, P. Yang, S. Yi, J. Rao and Y. Zhang, 1D-3D biological template loaded NiCo nanowires at high temperatures as a broadband, lightweight electromagnetic wave absorbing material, *Powder Technol.*, 2023, **426**, 118670.

23 C. Zhang, D. Wang, L. Dong, K. Li, Y. Zhang, P. Yang, S. Yi, X. Dai, C. Yin, Z. Du, X. Zhang, Q. Zhou, Z. Yi, J. Rao and Y. Zhang, Microwave Absorption of α-Fe2O3@diatomite Composites, *Int. J. Mol. Sci.*, 2022, **23**, 9362.

24 Z. Du, D. Wang, X. Zhang, Z. Yi, J. Tang, P. Yang, R. Cai, S. Yi, J. Rao and Y. Zhang, Core-Shell Structured SiO2@NiFe LDH Composite for Broadband Electromagnetic Wave Absorption, *Int. J. Mol. Sci.*, 2022, **24**, 504.

25 A. J. Tchinda, E. Ngameni, I. T. Kenfack and A. Walcarius, One-Step Preparation of Thiol-Functionalized Porous Clay Heterostructures: Application to Hg(II) Binding and Characterization of Mass Transport Issues, *Chem. Mater.*, 2009, **21**, 4111–4121.

26 W. Kiciński, M. Szala and M. Bystrzejewski, Sulfur-doped porous carbons: Synthesis and applications, *Carbon*, 2014, **68**, 1–32.

27 Q. Zou, L. Zou and H. Tian, Detection and adsorption of Hg2+ by new mesoporous silica and membrane material grafted with a chemodosimeter, *J. Mater. Chem.*, 2011, **21**, 14441.

28 D. M. Saad, E. M. Cukrowska and H. Tutu, Selective removal of mercury from aqueous solutions using thiolated cross-linked polyethylenimine, *Appl. Water Sci.*, 2013, **3**, 527–534.

29 M. Sharma, M. Joshi, S. Nigam, S. Shree, D. K. Avasthi, R. Adelung, S. K. Srivastava and Y. Kumar Mishra, ZnO

tetrapods and activated carbon based hybrid composite: Adsorbents for enhanced decontamination of hexavalent chromium from aqueous solution, *Chem. Eng. J.*, 2019, **358**, 540–551.

30 S. Mollick, S. Fajal, S. Saurabh, D. Mahato and S. K. Ghosh, Nanotrap Grafted Anion Exchangeable Hybrid Materials for Efficient Removal of Toxic Oxoanions from Water, *ACS Cent. Sci.*, 2020, **6**, 1534–1541.

31 X. Ma, L. Li, L. Yang, C. Su, K. Wang, S. Yuan and J. Zhou, Adsorption of heavy metal ions using hierarchical CaCO3-maltose meso/macroporous hybrid materials: adsorption isotherms and kinetic studies, *J. Hazard. Mater.*, 2012, **209–210**, 467–477.

32 Y. Zhang, X. Xu, A. Li, W. Liu and F. Liu, Enhanced and efficient removal of heavy metals by amino-decorated membranes in coordination with multi-function, *J. Water Process. Eng.*, 2023, **51**, 103328.

33 B. Li, Y. Zhang, D. Ma, Z. Shi and S. Ma, Mercury nano-trap for effective and efficient removal of mercury(II) from aqueous solution, *Nat. Commun.*, 2014, **5**, 5537.

34 B. Aguila, Q. Sun, J. A. Perman, L. D. Earl, C. W. Abney, R. Elzein, R. Schlaf and S. Ma, Efficient Mercury Capture Using Functionalized Porous Organic Polymer, *Adv. Mater.*, 2017, **29**, 1700665.

35 H. Hosseinzadeh, S. Hosseinzadeh and S. Pashaei, Fabrication of novel magnetic graphene oxide nanocomposites for selective adsorption of mercury from aqueous solutions, *Environ. Sci. Pollut. Res.*, 2019, **26**, 26807–26821.

36 V. J. Inglezakis, A. Kurbanova, A. Molkenova, A. A. Zorpas and T. S. Atabaev, Magnetic Fe3O4-Ag0 Nanocomposites for Effective Mercury Removal from Water, *Sustainability*, 2020, **12**, 5489.

37 J. Cheng, Y. Li, L. Li, P. Lu, Q. Wang and C. He, Thiol-/thioether-functionalized porous organic polymers for simultaneous removal of mercury(II) ion and aromatic pollutants in water, *New J. Chem.*, 2019, **43**, 7683–7693.

38 C. Long, X. Li, Z. Jiang, P. Zhang, Z. Qing, T. Qing and B. Feng, Adsorption-improved MoSe2 nanosheet by heteroatom doping and its application for simultaneous detection and removal of mercury (II), *J. Hazard. Mater.*, 2021, **413**, 125470.

39 A. Shahzad, J. Jang, S.-R. Lim and D. S. Lee, Unique selectivity and rapid uptake of molybdenum-disulfide-functionalized MXene nanocomposite for mercury adsorption, *Environ. Res.*, 2020, **182**, 109005.

40 T. Tene, F. Arias Arias, M. Guevara, A. Nuñez, L. Villamagua, C. Tapia, M. Pisarra, F. J. Torres, L. S. Caputi and C. Vacacela Gomez, Removal of mercury(II) from aqueous solution by partially reduced graphene oxide, *Sci. Rep.*, 2022, **12**(1), 6326.

41 N. M. Bandaru, N. Reta, H. Dalal, A. V. Ellis, J. Shapter and N. H. Voelcker, Enhanced adsorption of mercury ions on thiol derivatized single wall carbon nanotubes, *J. Hazard. Mater.*, 2013, **261**, 534–541.

42 W.-J. Shi, F.-M. Menn, T. Xu, Z. T. Zhuang, C. Beasley, S. Ripp, J. Zhuang, A. C. Layton and G. S. Sayler, C60 reduces the bioavailability of mercury in aqueous solutions, *Chemosphere*, 2014, **95**, 324–328.

43 R. S. Chouhan, I. Jerman, D. Heath, S. Bohm, S. Gandhi, V. Sadhu, S. Baker and M. Horvat, Emerging tri-s-triazine-based graphitic carbon nitride: A potential signal-transducing nanostructured material for sensor applications, *Nano Sel.*, 2021, **2**, 712–743.

44 J. Bian, C. Huang and R.-Q. Zhang, Graphitic Carbon Nitride Film: An Emerging Star for Catalytic and Optoelectronic Applications, *ChemSusChem*, 2016, **9**, 2723–2735.

45 Y. Zheng, J. Liu, J. Liang, M. Jaroniec and S. Z. Qiao, Graphitic carbon nitride materials: controllable synthesis and applications in fuel cells and photocatalysis, *Energy Environ. Sci.*, 2012, **5**, 6717.

46 A. Wang, C. Wang, L. Fu, W. Wong-Ng and Y. Lan, Recent Advances of Graphitic Carbon Nitride-Based Structures and Applications in Catalyst, Sensing, Imaging, and LEDs, *Nano-Micro Lett.*, 2017, **9**, 47.

47 L. Chen and J. Song, Tailored Graphitic Carbon Nitride Nanostructures: Synthesis, Modification, and Sensing Applications, *Adv. Funct. Mater.*, 2017, **27**, 1702695.

48 R. S. Chouhan, G. Žitko, V. Fajon, I. Živković, M. Pavlin, S. Berisha, I. Jerman, A. Vesel and M. Horvat, A Unique Interactive Nanostructure Knitting based Passive Sampler Adsorbent for Monitoring of Hg^{2+} in Water, *Sensors*, 2019, **19**, 3432.

49 M. Shi, X. Yang and W. Zhang, Magnetic graphitic carbon nitride nano-composite for ultrasound-assisted dispersive micro-solid-phase extraction of Hg(II) prior to quantitation by atomic fluorescence spectroscopy, *Anal. Chim. Acta*, 2019, **1074**, 33–42.

50 S. Kumar, S. Tonda, B. Kumar, A. Baruah and V. Shanker, Synthesis of Magnetically Separable and Recyclable g-C 3 N 4 –Fe3 O4 Hybrid Nanocomposites with Enhanced Photocatalytic Performance under Visible-Light Irradiation, *J. Phys. Chem. C*, 2013, **117**, 26135–26143.

51 Q. Liang, L. Yu, W. Jiang, S. Zhou, S. Zhong and W. Jiang, One-pot synthesis of magnetic graphitic carbon nitride photocatalyst with synergistic catalytic performance under visible-light irradiation, *J. Photochem. Photobiol., A*, 2017, **335**, 165–173.

52 Y. Li, J. Zhang, Q. Wang, Y. Jin, D. Huang, Q. Cui and G. Zou, Nitrogen-Rich Carbon Nitride Hollow Vessels: Synthesis, Characterization, and Their Properties, *J. Phys. Chem. B*, 2010, **114**, 9429–9434.

53 K. Gibson, J. Glaser, E. Milke, M. Marzini, S. Tragl, M. Binnewies, H. A. Mayer and H.-J. Meyer, Preparation of carbon nitride materials by polycondensation of the single-source precursor aminodichlorotriazine (ADCT), *Mater. Chem. Phys.*, 2008, **112**, 52–56.

54 S. Liu, K. Yao, L. H. Fu and M. G. Ma, Selective synthesis of Fe3O4, γ-Fe2O3, and α-Fe2O3 using cellulose-based composites as precursors, *RSC Adv.*, 2016, **6**, 2135–2140.

55 H. Shagholani, S. M. Ghoreishi and M. Mousazadeh, Improvement of interaction between PVA and chitosan *via* magnetite nanoparticles for drug delivery application, *Int. J. Biol. Macromol.*, 2015, **78**, 130–136.

56 E. Hee Kim, H. Sook Lee, B. Kook Kwak and B.-K. Kim, Synthesis of ferrofluid with magnetic nanoparticles by sonochemical method for MRI contrast agent, *J. Magn. Magn. Mater.*, 2005, **289**, 328–330.

57 A. Raza, H. Shen, A. A. Haidry and S. Cui, Hydrothermal synthesis of Fe3O4/TiO2/g-C3N4: Advanced photocatalytic application, *Appl. Surf. Sci.*, 2019, **488**, 887–895.

58 A. A. Haidry and L. Sun, in *Functional Reverse Engineering of Machine Tools*, 2019.

59 S. Sun, X. Gou, S. Tao, J. Cui, J. Li, Q. Yang, S. Liang and Z. Yang, Mesoporous graphitic carbon nitride (g-C 3 N 4) nanosheets synthesized from carbonated beverage-reformed commercial melamine for enhanced photocatalytic hydrogen evolution, *Mater. Chem. Front.*, 2019, **3**, 597–605.

60 J.-H. Zhang, Y.-J. Hou, S.-J. Wang, X. Zhu, C.-Y. Zhu, Z. Wang, C.-J. Li, J.-J. Jiang, H.-P. Wang, M. Pan and C.-Y. Su, A facile method for scalable synthesis of ultrathin g-C 3 N 4 nanosheets for efficient hydrogen production, *J. Mater. Chem. A*, 2018, **6**, 18252–18257.

61 D. A. Erdogan, M. Sevim, E. Kısa, D. B. Emiroglu, M. Karatok, E. I. Vovk, M. Bjerring, Ü. Akbey, Ö. Metin and E. Ozensoy, Photocatalytic Activity of Mesoporous Graphitic Carbon Nitride (mpg-C3N4) Towards Organic Chromophores Under UV and VIS Light Illumination, *Top. Catal.*, 2016, **59**, 1305–1318.

62 L. Lin, H. Ou, Y. Zhang and X. Wang, Tri-s-triazine-Based Crystalline Graphitic Carbon Nitrides for Highly Efficient Hydrogen Evolution Photocatalysis, *ACS Catal.*, 2016, **6**(6), 3921–3931.

63 D. Zhao, C. Dong, B. Wang, C. Chen, Y. Huang, Z. Diao, S. Li, L. Guo and S. Shen, Synergy of Dopants and Defects in Graphitic Carbon Nitride with Exceptionally Modulated Band Structures for Efficient Photocatalytic Oxygen Evolution, *Adv. Mater.*, 2019, **31**, 1903545.

64 C. H. Choi, L. Lin, S. Gim, S. Lee, H. Kim, X. Wang and W. Choi, Polymeric Carbon Nitride with Localized Aluminum Coordination Sites as a Durable and Efficient Photocatalyst for Visible Light Utilization, *ACS Catal.*, 2018, **8**, 4241–4256.

65 J. Xu, J.-K. Shang, Q. Jiang, Y. Wang and Y.-X. Li, Facile alkali-assisted synthesis of g-C 3 N 4 materials and their high-performance catalytic application in solvent-free cycloaddition of CO 2 to epoxides, *RSC Adv.*, 2016, **6**, 55382–55392.

66 A. S. Krishna Kumar, J.-G. You, W.-B. Tseng, G. D. Dwivedi, N. Rajesh, S.-J. Jiang and W.-L. Tseng, Magnetically Separable Nanospherical g-C 3 N 4 @Fe 3 O 4 as a Recyclable Material for Chromium Adsorption and Visible-Light-Driven Catalytic Reduction of Aromatic Nitro Compounds, *ACS Sustainable Chem. Eng.*, 2019, **7**, 6662–6671.

67 G. Perez, M. P. Romero, E. B. Saitovitch, F. J. Litterst, J. F. D. F. Araujo, D. C. Bell and G. Solorzano, Alkali concentration effects on the composition, morphology and magnetic properties of magnetite, maghemite and iron oxyhydroxide nanoparticles, *Solid State Sci.*, 2020, **106**, 106295.

68 X. Zhang, W. Jiang, X. Gong and Z. Zhang, Sonochemical synthesis and characterization of magnetic separable Fe3O4/Ag composites and its catalytic properties, *J. Alloys Compd.*, 2010, **508**, 400–405.

69 L. Zhuang, W. Zhang, Y. Zhao, H. Shen, H. Lin and J. Liang, Preparation and characterization of Fe3O4 particles with novel nanosheets morphology and magnetochromatic property by a modified solvothermal method, *Sci. Rep.*, 2015, **5**, 9320.

70 F. Fina, S. K. Callear, G. M. Carins and J. T. S. Irvine, Structural Investigation of Graphitic Carbon Nitride *via* XRD and Neutron Diffraction, *Chem. Mater.*, 2015, **27**, 2612–2618.

71 S. K. Lakhera, R. T. Pangal, H. Y. Hafeez and B. Neppolian, Oxygen-Functionalized and Ni+x (x=2, 3)-Coordinated Graphitic Carbon Nitride Nanosheets with Long-Life Deep-Trap States and their Direct Solar-Light-Driven Hydrogen Evolution Activity, *ChemSusChem*, 2019, **12**, 4293–4303.

72 Y. P. Yew, K. Shameli, M. Miyake, N. B. B. Ahmad Khairudin, S. E. B. Mohamad, H. Hara, M. F. B. Mad Nordin and K. X. Lee, An Eco-Friendly Means of Biosynthesis of Superparamagnetic Magnetite Nanoparticles *via* Marine Polymer, *IEEE Trans. Nanotechnol.*, 2017, **16**, 1047–1052.

73 S. R. Guevara, S. Žižek, U. Repinc, S. P. Catán, R. Jaćimović and M. Horvat, *Anal. Bioanal. Chem.*, 2007, **387**(6), 2185–2197.

74 J.-H. Park, J. J. Wang, B. Zhou, J. E. R. Mikhael and R. D. DeLaune, Removing mercury from aqueous solution using sulfurized biochar and associated mechanisms, *Environ. Pollut.*, 2019, **244**, 627–635.

75 R. Madhuvilakku, S. Alagar, R. Mariappan and S. Piraman, Green one-pot synthesis of flowers-like Fe3O4/rGO hybrid nanocomposites for effective electrochemical detection of riboflavin and low-cost supercapacitor applications, *Sens. Actuators, B*, 2017, **253**, 879–892.

76 S. Guo, N. Duan, Z. Dan, G. Chen, F. Shi and W. Gao, g-C3N4 modified magnetic Fe3O4 adsorbent: Preparation, characterization, and performance of Zn(II), Pb(II) and Cd(II) removal from aqueous solution, *J. Mol. Liq.*, 2018, **258**, 225–234.

77 R. Rahmi, F. Fathurrahmi, L. Lelifajri and F. PurnamaWati, Preparation of magnetic chitosan using local iron sand for mercury removal, *Heliyon*, 2019, **5**, e01731.

78 C. Zhou, H. Zhu, Q. Wang, J. Wang, J. Cheng, Y. Guo, X. Zhou and R. Bai, Adsorption of mercury(II) with an Fe_3O_4 magnetic polypyrrole–graphene oxide nanocomposite, *RSC Adv.*, 2017, **7**, 18466–18479.

79 S. Zhang, Y. Zhang, J. Liu, Q. Xu, H. Xiao, X. Wang, H. Xu and J. Zhou, Thiol modified Fe3O4@SiO2 as a robust, high effective, and recycling magnetic sorbent for mercury removal, *Chem. Eng. J.*, 2013, **226**, 30–38.

80 S. M. Husnain, J.-H. Kim, C.-S. Lee, Y.-Y. Chang, W. Um and Y.-S. Chang, Superparamagnetic nalidixic acid grafted magnetite (Fe3 O4/NA) for rapid and efficient mercury removal from water, *RSC Adv.*, 2016, **6**, 35825–35832.

81 A. Srikhaow, T. Butburee, W. Pon-On, T. Srikhirin, K. Uraisin, K. Suttiponpanit, S. Chaveanghong and S. M. Smith, Efficient Mercury Removal at Ultralow Metal Concentrations

by Cysteine Functionalized Carbon-Coated Magnetite, *Appl. Sci.*, 2020, **10**, 8262.

82 M. E. Fernandez, B. Ledesma, S. Román, P. R. Bonelli and A. L. Cukierman, Development and characterization of activated hydrochars from orange peels as potential adsorbents for emerging organic contaminants, *Bioresour. Technol.*, 2015, **183**, 221–228.

83 D. Chen, H. Zhang, K. Yang and H. Wang, Functionalization of 4-aminothiophenol and 3-aminopropyltriethoxysilane with graphene oxide for potential dye and copper removal, *J. Hazard. Mater.*, 2016, **310**, 179–187.

84 M. R. Awual, Novel nanocomposite materials for efficient and selective mercury ions capturing from wastewater, *Chem. Eng. J.*, 2017, **307**, 456–465.